Chapter 4

Role of Na^+ co-doping in luminescence enhancement of Bi_2O_3: Sm^{3+} nanophosphors

In this chapter, we present a comprehensive structural and optical study of alkali metal ion (Na^+) co-doping in samarium-doped bismuth oxide nanophosphors and its role in enhancing the red emission of the phosphors. X-ray diffraction (XRD) analysis ascertains the monoclinic crystal structure. The XRD analysis also reveals an improvement in crystallinity after Na^+ co-doping. The HR-SEM micrographs reveal the nanosheet-like morphology and the EDX spectroscopy confirms the presence of all elements in the prepared phosphors. The TEM analysis validates the structural and morphological findings. The UV-Vis-NIR spectroscopic analysis has been carried out to estimate the bandgap as well as to investigate the Urbach energy of the phosphors. An augmentation in bandgap energy (2.784 to 2.807 eV) is observed for lower Na^+ co-doping in samarium doped phosphor and shows a decreasing trend with increasing Na^+ concentration. The room temperature photoluminescence (PL) emission studies were performed under 481 nm excitation. Nearly ten-fold enhancement in the emission intensity was observed in the optimized Bi_2O_3:(5%)Sm^{3+} with co-doping of 1% Na^+ ions. The lifetime of the $^4G_{5/2}$ level of the Sm^{3+} ions has also increased on doping 1% Na^+ ions. The thermal stability of the phosphors has been investigated using temperature-dependent PL analysis over the temperature range of 303-453 K. The correlated color temperature (CCT) analysis reveals that the prepared nanophosphors are promising and potential red-emitting phosphors to realize efficient optoelectronic and display devices.

4.1 Introduction

In recent years, metal oxide nanostructures have drawn the special interest of the scientific community owing to their fascinating and intriguing attributes such as thermal stability, biocompatibility, mechanical strength, environment-friendly nature, ferroelectric properties, and quantum size effects [90,91] and shown technologically important and pervading applications such as nanomedicines for therapeutics and diagnostics, electrochemical sensors for the detection of biomolecules, antibacterial activity, electrode material for supercapacitor application and as a convenient luminescence host for fluorescence devices and so on [92–96].

Among various metal oxides, bismuth oxide (Bi_2O_3) is considered an exquisite nanomaterial owing to its remarkable and noteworthy features such as non-toxicity, photocatalytic activity, chemical stability, high refractive index, wide bandgap, and extraordinary optical and electrical properties [97]. Bi_2O_3 exhibits polymorphic nature and exists in several polymorphic forms [98]. Among them, α-Bi_2O_3 with a monoclinic crystal structure is highly stable at room temperature and instigates its applications as anode material for energy storage devices and solar cell applications [99,100]. Apart from that, bismuth oxide has also been a material of choice as a luminescence host for various activator and co-activator ions *viz*: rare-earth ions, alkali metals, transition metal ions, etc. Bi_2O_3 can be synthesized via various synthesis routes such as solution combustion, probe sonication, co-precipitation, hydrothermal, and sol-gel methods [101–105]. Among them, the co-precipitation method is popularly known to be a robust, viable, inexpensive, momentous, environmentally benign, and ingenious method, used for the size-controlled synthesis of nanophosphors at low reaction temperatures and within a short period of time.

In the last few years, rare-earth-doped metal oxide nanostructures have been extensively explored by various research groups owing to their multifarious applications in sensors, display, and optoelectronic devices [106–108]. Rare earth-doped bismuth oxide nanostructures have shown novel applications in a variety of disciplines such as photocatalysts for the removal of organic contaminants, fibers, temperature sensors, etc. [53,109,110]. Usually, Bi_2O_3 exhibits a broad and weak emission band in the visible region, ranging from 400-650 nm [111], which limits its applications in lighting, and display devices. Therefore, several efforts have been devoted to augment the fluorescence emission intensity of bismuth oxide nanophosphors by doping a wide range of rare-earth ions. J. Divya *et al.* have synthesized Ho^{3+} doped Bi_2O_3 needles and studied their photocatalytic and emission properties [69]. S. Ashwini *et al.* have prepared novel Bi_2O_3:Tb^{3+} green-emitting nanophosphors and discussed their applications in display devices and forensic analysis [89]. Liumin Fan *et al.* have synthesized Sm^{3+} doped Bi_2O_3 nanophosphors using the solid-state reaction method and shown its multitudinous applications in photodetection, temperature sensing, and light-shielding [53].

It has been found that co-doping of different co-activator ions such as alkali metals, alkaline earth metals, and transition metal ions in different host materials can boost the fluorescence intensity of rare-earth-doped phosphors [112]. P. S. David *et al.* have shown the luminescence enhancement mechanism in Yb^{3+} and Bi^{3+} co-doped $Zn_xNb_{(1-x)}O$ composite synthesized for silicon solar cell applications [113]. Pawan Kumar *et al.* have demonstrated the enhanced luminescence and ferromagnetism in Eu^{3+} doped zinc oxide via Li^+ co-doping [50]. Pramod *et al.* have studied the structural and fluorescence properties of Li^+, Na^+ and K^+ co-doped and Eu^{3+} activated $GdPO_4$ phosphors [114]. Ruby Priya *et al.* have investigated the spectroscopic properties of alkaline-earth metal-doped Gd_2O_3:Eu phosphors synthesized via co-precipitation method and discussed the variations in its

structural and optical properties [115]. Facile sol-gel synthesis and characterization of Mn and Nd co-doped ZnO nanoparticles have been presented by A. Albert Manoharan *et al.* [116]. The role of charge compensators (Li^+, Na^+, and K^+) in the luminescence enhancement of Bi^{3+}-doped $CaSb_2O_6$ phosphors has been explored by S. Yao *et al.* [117]. Vaibhav *et al.* have reported 1.5 times enhancement in fluorescence intensity of Sm- doped $SrMoO_4$ phosphors via the co-doping Bi^{3+} ions [88].

The present chapter provides a comprehensive study of the effects of Na^+ ion co-doping on Sm^{3+} doped Bi_2O_3 nanophosphors synthesized via the co-precipitation method. The structural and optical properties of the phosphors and their correlations have been discussed in detail. It is observed that the Na^+/Sm^{3+} co-doped Bi_2O_3 nanophosphors have emission in the red region, which makes it potential candidate as a red phosphor in different optoelectronic, lighting, and display devices. Moreover, the temperature-dependent PL analysis suggests the thermal stability of the phosphors at high temperatures.

4.2 Experimental section

4.2.1 Materials and methods

A series of Bi_2O_3:Sm^{3+} and Na^+ co-doped Bi_2O_3:Sm^{3+} nanophosphors have been synthesized by co-precipitation method. In this series, we have synthesized Bi_2O_3 host, Sm^{3+} (1-7 %) doped Bi_2O_3 and Sm^{3+} (5%) doped, Na^+ (0.3, 0.5, 1, 3 and 5%) co-doped Bi_2O_3 and encoded them as SB0, SB1, SB3, SB5, SB7, SBN0.3, SBN0.5, SBN1, SBN3 and SBN5, respectively. The starting materials used for synthesis were $Bi(NO_3)_3 \cdot 5H_2O$ (Sigma-Aldrich, 98%), $Sm(NO_3)_3$, Sigma-Aldrich, 99.999%), $NaNO_3$ (Sigma-Aldrich, ≥ 99%), and NaOH (SRL, 98%). The detailed synthesis process of the phosphors has been elucidated in our previous work [103].

4.3 Characterizations

X-ray diffraction (XRD) analysis is a prevalent tool to estimate the crystal structure and authenticate the phase purity of unknown samples. The XRD spectra of the samples were recorded over the range of $20° \leq 2\theta \leq 70°$ using benchtop X-ray diffraction (BT-XRD) **(**Model: miniflex 600 desktop X-ray diffraction system, Company: RIGAKU Corporation) attired with Cu-K_α source of monochromatic radiation (λ = 1.54 Å), operating at 15 mA and 30 kV. The high-resolution scanning electron microscopic (HR-SEM) analysis, equipped with energy dispersive X-ray (EDX) spectrometer was performed using Nova Nano SEM 450, FEI Company of USA (S.E.A.) PTE, LTD. The transmission electron microscopy (TEM) and selected area electron diffraction (SAED) patterns were recorded with the help of Tecnai G2 20 TWIN (FEI) instrument. The X-ray photoelectron spectroscopic analysis (XPS), a surface-sensitive technique has been used to explore the composition of chemical species, the detection of elements present in the samples, and further estimate their oxidation states. The XPS of samples were investigated using k-alpha company- Thermo Fisher Scientific. The UV-Vis-NIR spectroscopy of the phosphors was recorded over the wavelength range of 200-1000 nm using JASCO V-770 spectrophotometer. The Fourier transform infrared (FTIR) spectra of the samples were accomplished using JASCO FT/IR-4600 spectrometer. The PL excitation and emission spectra, and the temperature-dependent luminescence of the nanophosphors were examined with the help of Horiba Fluorolog-3 spectrofluorometer furnished with a 450 W xenon flash lamp. The luminescence decay curves were recorded using FS5 spectrofluorometer.

4.4 Results and discussion

4.4.1 Structural analysis

The powder XRD (PXRD) analysis was employed to investigate the crystal structure of the phosphors. The Rietveld refined XRD pattern of Bi_2O_3 host, obtained using FULLPROF software is depicted in Fig. 4.1 (a) and the corresponding refinement parameters *viz.* - atomic positions, lattice parameters, unit cell volume, and $R_{Factors}$ are summarized in Table 4.1. The crystal structure of bismuth oxide obtained with the help of VESTA program is illustrated in Fig. 4.1 (b). It contains two Bi (Bi1 and Bi2) and three oxygen (O1, O2, and O3) atoms located at respective 4e Wyckoff sites. The two Bi atoms show five and six-fold coordination with the neighboring oxygen atoms, respectively [118]. Fig. 4.2 shows the stacked XRD pattern of SB0, SB5, and SBN1 nanophosphors, calcined at 600 ^oC. The peak indexing was done in accordance with the standard Bragg's positions (JCPDS card no. 41-1449) having space group $P2_1/c$ and was found consistent with the monoclinic crystal structure of bismuth oxide nanoparticles. However, few impurity peaks with low intensity were observed in doped and co-doped samples, which correspond to bismuth samarium oxide [denoted by $ in Fig. 4.2]. The lattice parameters, interfacial angle (β), and unit cell volume (V) of the samples were estimated by unitCell software and the respective values are listed in Table 4.2. The decrease in cell volume in Na^+ co-doped samples can be ascribed to the substitution at the lattice sites. As the ionic radius of Na^+ (1.02Å) ions is comparable to the Bi^{3+} (1.03Å) ions, it is expected that they can be easily embedded in the host lattice and accommodate the substitutional sites. The substitution leads to a decrease in the lattice parameters and a shrinkage in the crystal cell volume. The particle density for the samples has been calculated using the formula [54],

$$\rho_{cal} = \frac{ZM}{NV} \tag{4.1}$$

Where, Z (= 4) is the formula unit for Bi_2O_3, M represents the molecular weight, $N(6.02214 \times 10^{23})$ is the Avogadro number and V is the unit cell volume. The decrease in particle density in co-doped samples also confirms the substitution at host sites.

The well known Debye-Scherrer formula used to estimate the average crystallite size of the phosphors is given as,

$$D = \frac{0.9\lambda}{\beta cos\theta} \tag{4.2}$$

Where, λ (= 1.54 Å) is the wavelength of incident monochromatic X-ray radiation, β (in radian) is the full width at half maximum (FWHM) and θ is the corresponding peak position at which diffraction occurs. The obtained crystallite size values are listed in Table 4.2, which suggests that the doping of Sm^{3+} ions in the host lattice results in a decrease in the crystallite size [85,119] whereas, the crystallite size increases in Na^+ co-doped samples. The co-doping of Na^+ in the lattice alleviates the density of grain boundaries. The grain boundaries act as light adsorption or scattering sites, which might restrain the grain growth and also act as luminescence quenching centers. Therefore, the co-doping of Na^+ favours the grain growth and leads to an augmentation in the size of the crystallite and also an enhancement in the photoluminescence [120,121].

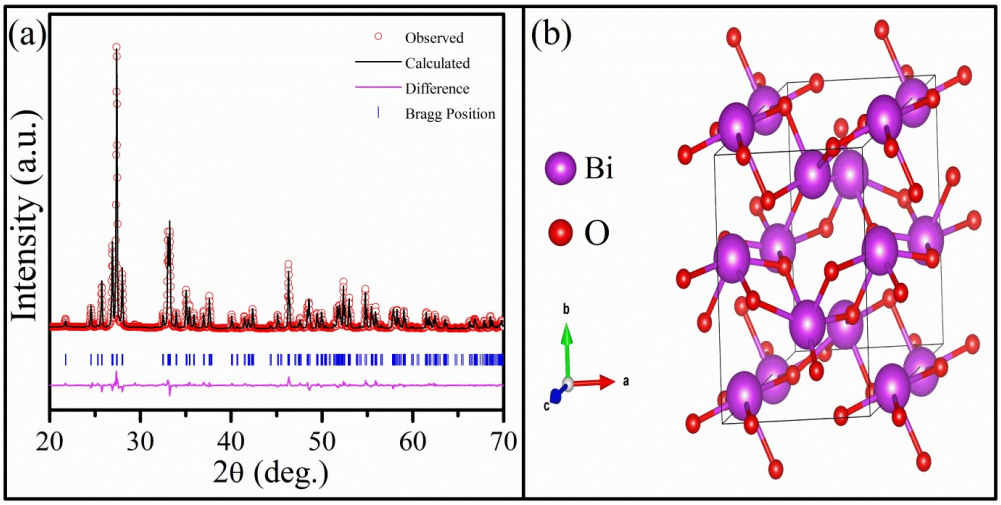

Fig. 4.1 (a) Rietveld refined XRD pattern and **(b)** The monoclinic crystal structure of SB0.

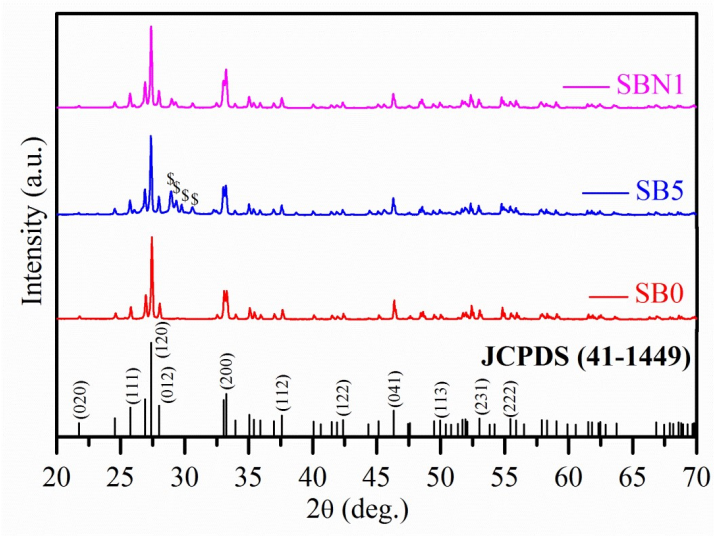

Fig. 4.2 Stacked XRD pattern of SB0, SB5 and SBN1.

Table 4.1 Atomic positions, lattice parameters, Unit cell volume, and $R_{Factors}$ obtained after Rietveld refinement for bismuth oxide (SB0).

Parameters	**SB0**
Atomic positions	
Bi1 (x,y,z)	(0.5246,0.1823,0.3618)
Bi2 (x,y,z)	(0.0416,0.0425,0.7767)
O1 (x,y,z)	(0.7154,0.2873,0.6343)
O2 (x,y,z)	(0.2565,0.0229,0.1193)
O3 (x,y,z)	(0.2376,0.0443,0.5122)
Angles (α, β, γ) in degree	(90, 112.982, 90)
Lattice parameters (Å)	
A	5.8512
B	8.1702
C	7.5139
Unit cell volume $(Å^3)$	330.69
$R_{Factors}$	
R_p	10.7
R_{wp}	11.8
R_{exp}	4.24
χ^2	7.75

Table 4.2 Lattice parameters, Interfacial angle (β), Unit cell volume (V), calculated particle density (ρ_{cal}), and average crystallite size (D) for all the samples.

Sample	Lattice parameters (Å)			β (deg.)	V $(Å)^3$	ρ_{cal} (g/cm^3)	D (nm)
	a	b	c				
SB0	5.8448	8.1595	7.5017	112.98	329.37	9.39	64.97
SB1	5.8528	8.1688	7.5132	113.00	330.65	9.34	60.31
SB3	5.8485	8.1635	7.5054	112.95	329.98	9.31	58.95
SB5	5.8568	8.1735	7.5190	113.01	331.30	9.22	58.32
SB7	5.8425	8.1591	7.4964	112.88	329.23	9.23	49.76
SBN0.3	5.8530	8.1688	7.5191	113.11	330.65	9.22	59.44
SBN0.5	5.8522	8.1686	7.5135	113.00	330.62	9.21	60.76
SBN1	5.8474	8.1683	7.5091	113.12	329.85	9.19	61.55
SBN3	5.8464	8.1637	7.5021	112.99	329.62	9.05	62.00
SBN5	5.8450	8.1590	7.4976	112.90	329.38	8.90	62.61

4.4.2 HR-SEM and EDX analysis

The surface morphology of the phosphors has been investigated by HR-SEM images. Figs. 4.3 (a, c) depict the HR-SEM micrographs of the SB5 and SBN1 nanophosphors, respectively, and ascertain the nanosheet-like morphology of the phosphors with some agglomeration. The average thickness of nanosheets for SB5 and SBN1 phosphors was estimated using ImageJ software and found to be 23.33 and 45.42 nm, respectively, and the corresponding variations are shown by histograms given in Figs. 4.3 (b, d). The elemental analysis of the phosphors was carried out using EDX spectroscopy. Figs. 4.4 (a, b) validate the presence of all the elements in doped and co-doped phosphors (SB5 and SBN1) and confirm that the samples are formed in the pure state without the existence of any foreign element. The Atomic and weight percentage of the chemical constituents in

both the phosphors, obtained from EDX data and their stoichiometric amounts used in the synthesis are tabulated in Table 4.3 and found in good agreement with each other.

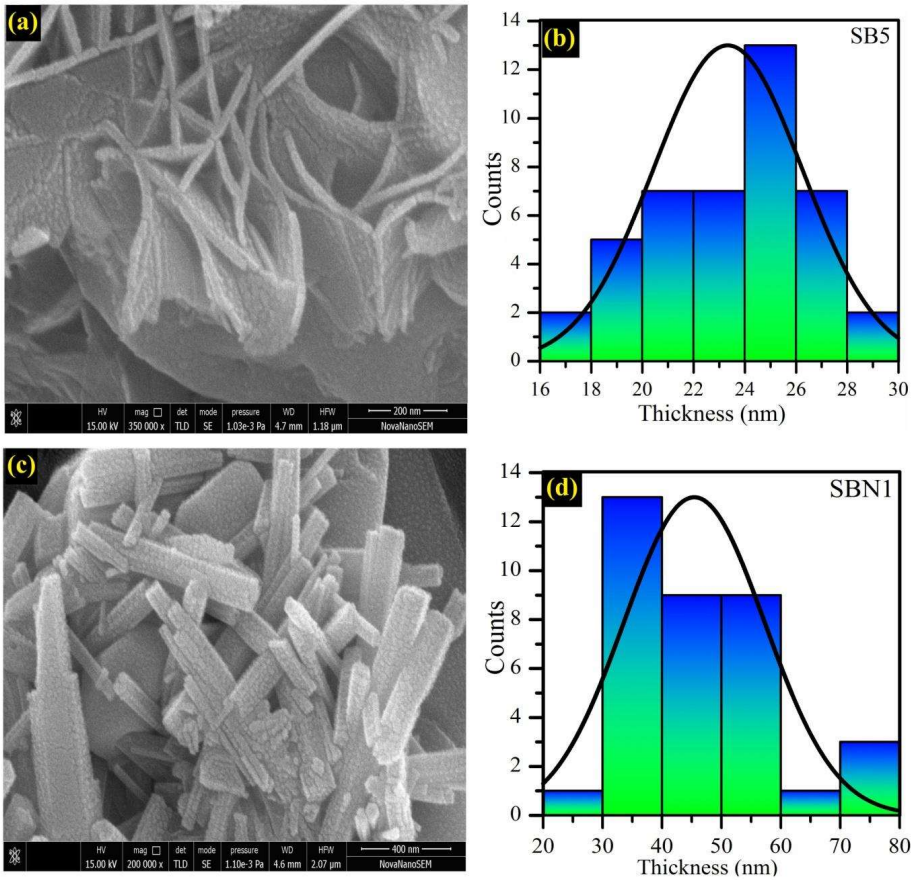

Fig. 4.3 (a, c) HR-SEM micrographs and **(b, d)** corresponding histograms of SB5 and SBN1 nanophosphors.

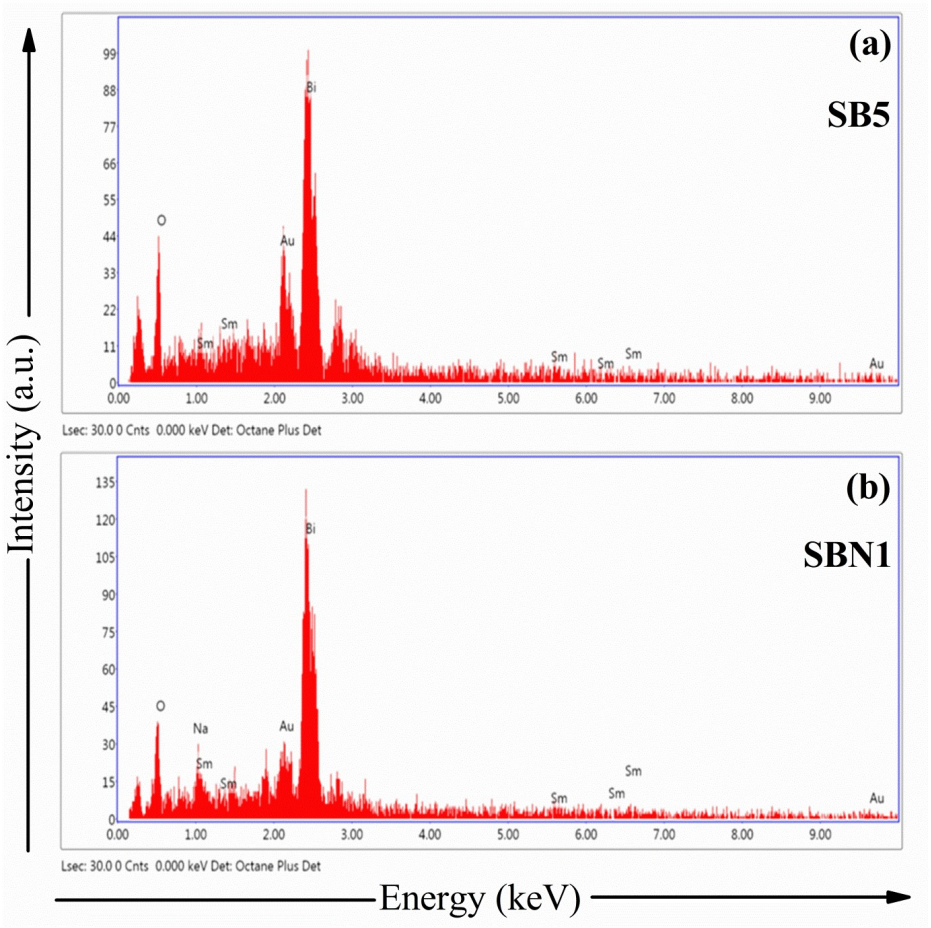

Fig. 4.4 EDX spectra of (a) SB5 and (b) SBN1 phosphors.

Table 4.3 Atomic % and weight % of elements present in SB5 and SBN1 obtained from EDX data and the stoichiometric amount used in the synthesis process.

Sample	Elements	Stoichiometric amount		Obtained from EDX	
		At. %	Wt.%	At. %	Wt.%
SB5	Bi	38	86.30	37.04	85.15
	Sm	2	3.26	2.55	4.22
	O	60	10.44	60.41	10.63
SBN1	Bi	37.6	86.09	36.27	84.96
	Sm	2	3.29	2.44	4.10
	Na	0.4	0.1	0.80	0.21
	O	60	10.52	62.10	11.14

4.4.3 TEM analysis

The morphology and phase of the phosphors were further confirmed by TEM analysis. Figs. 4.5 (a and c) illustrate the TEM images of SB5 and SBN1 nanophosphors, respectively, and validate the nanosheet-like morphology of the prepared samples, as obtained from the HR-SEM micrographs. The diffraction rings shown in the SAED pattern (Figs. 4.5 (b and d)) are indexed as (120), (200), (041), (024), (233) planes for SB5 and (120), (130), (041), (014), (232), (260) planes for SBN1 nanophosphors, respectively. The obtained diffraction planes match well with the XRD pattern and confirm the polycrystalline nature of the phosphors.

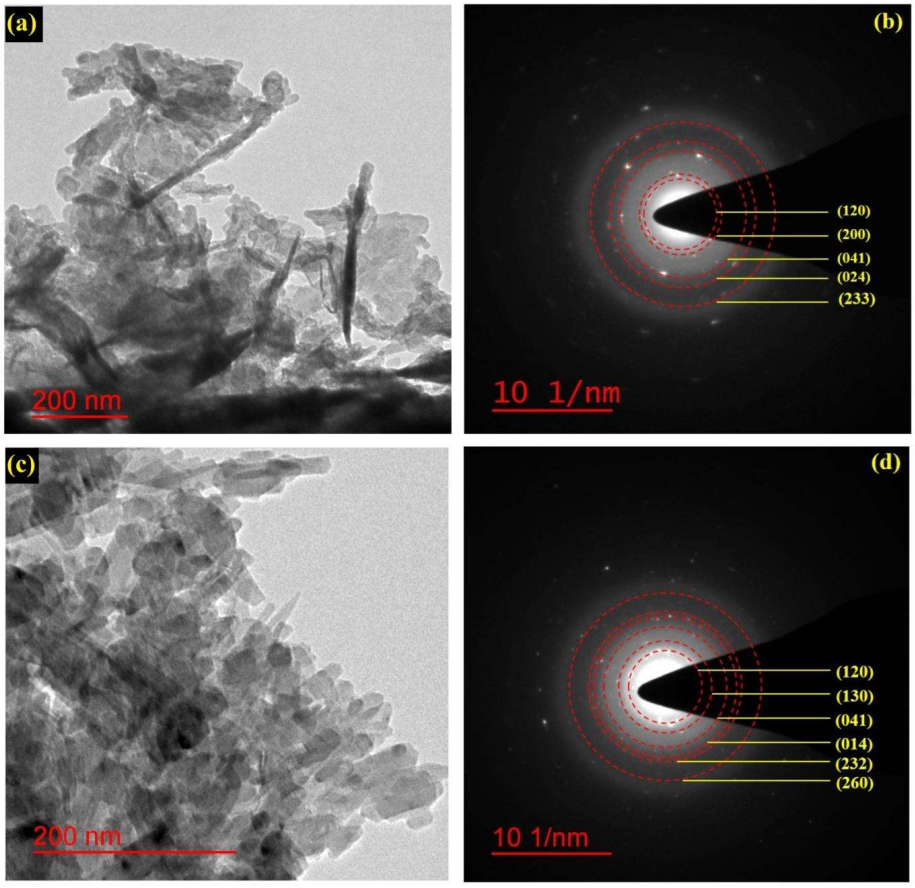

Fig. 4.5 (a, b) TEM images and **(b, d)** SAED patterns of SB5 and SBN1 nanophosphors.

4.4.4 XPS analysis

XPS is a surface characterization tool, used to examine the chemical constituents, oxidation states, and to confirm the existence of all the elements in the samples. The XPS spectrum of the SBN1 nanophosphor is displayed in Fig. 4.6 (a-e). The binding energy peaks of all the elements were charge corrected for C 1s (~284.7 eV) [67]. The Shirley-type background subtraction followed by Gaussian-Lorentzian peak fitting was employed to fit the peaks using XPSPEAK41 software. The XPS survey scan (Fig. 4.6 (a)) ascertains the presence of all the elements in the co-doped samples. Fig. 4.6 (b) depicts the peak fitted at ~1071.2 eV binding energy, which is attributed to the Na 1s peak and corresponds to the +1 oxidation state of Na [122]. The core-level spectrum of bismuth (Bi) ion is demonstrated

in Fig. 4.6 (c). The bands centered at ~158.7 and ~164.0 eV are ascribed to Bi $4f_{7/2}$ and Bi $4f_{5/2}$, respectively, and confirm the +3 oxidation state of Bi in the sample [54]. The high-resolution XPS spectra of O 1s (Fig. 4.6 (d)) is resolved into three peaks centered at ~529.4, ~531.0, and ~532.6 eV corresponding to lattice oxygen, oxygen vacancies (V_o), and surface adsorbed oxygen [123,124]. Thus, the XPS analysis validates the existence of oxygen vacancies in the samples. Fig. 4.6 (e) is showing the XPS spectra of samarium ion corresponding to +3 oxidation state and the peaks at ~1082.7 and ~1109.7 eV are allocated $3d_{5/2}$ and $3d_{3/2}$ core levels of samarium ion, respectively [54].

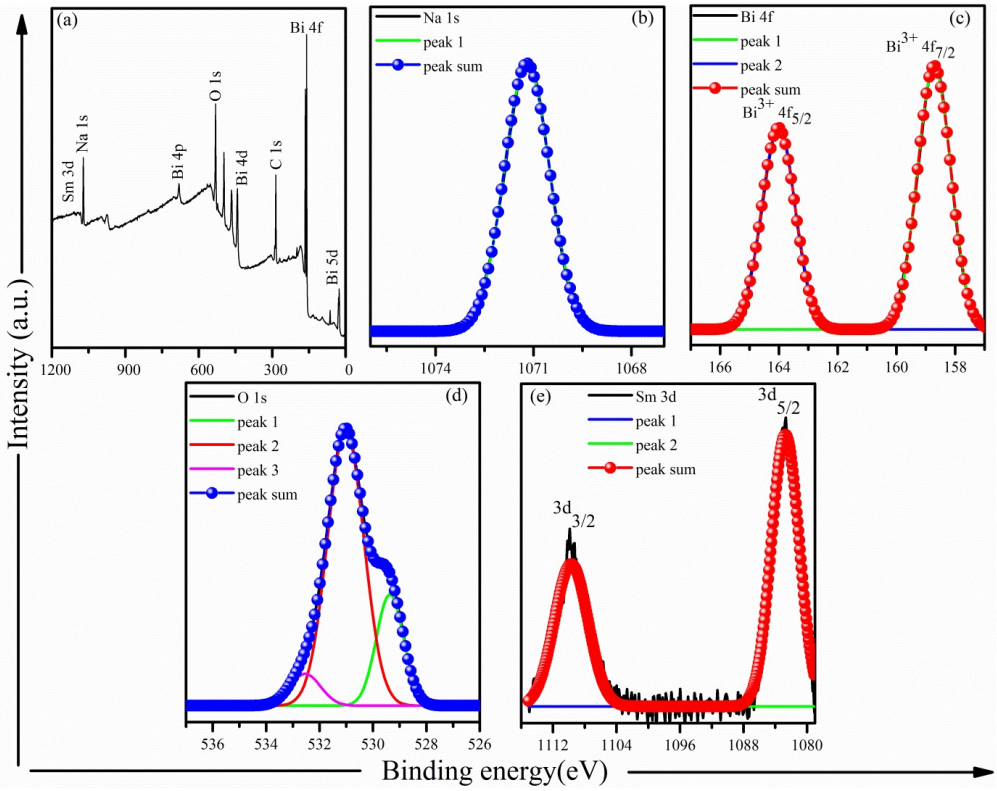

Fig. 4.6 (a) Full spectrum XPS survey scan, and high-resolution XPS spectra of **(b)** Na 1s **(c)** Bi 4f **(d)** O 1s and **(e)** Sm 3d for SBN1 nanophosphor.

4.4.5 Absorption study

The UV-Vis-NIR spectrophotometry is a prevalent optical characterization tool, employed to determine the optical band gap, Urbach energy, and the absorption behaviour of the phosphors in a definite region. The absorption spectra of the synthesized

nanophosphors, ranging from 200-1000 nm are presented in Fig. 4.8 (a, c). Band gap energy of the phosphors was estimated using the Tauc plots (Fig. 4.8 (b, d)) and the corresponding Tauc relation is given by [70,125],

$$(\alpha h\nu)^{1/n} = C(h\nu - E_g) \tag{4.3}$$

Where C is a constant, α denotes the coefficient of absorption, E_g is the optical band gap, n is the power factor, and $h\nu$ represents the incident photon energy. The value of n determines the type of the possible electronic transitions during the photon-absorption process. Its value is equal to 1/2, 2, 3/2, and 3, for direct allowed, indirect allowed, direct forbidden, and indirect forbidden transitions, respectively [50,126]. In order to determine the precise value of n for the samples, we take the natural logarithm and first order derivative of the equation (4.3) to get[127] :

$$\ln(\alpha h\nu) = ln\, C + n \ln(h\nu - E_g) \tag{4.4}$$

$$\frac{d \ln(\alpha h\nu)}{d(h\nu)} = \frac{n}{h\nu - E_g} \tag{4.5}$$

In our samples, we found the type of transition to be the direct allowed type ($n \approx 1/2$) (Table 4.4) [53]. The detailed calculation process of the power factor n and the corresponding plots (Figs.4.7(a), (b)) for SB0, SB5, and SBN1 phosphors are reported here[127]. According to the Eq. (4.5), if we plot a graph between $d \ln(\alpha h\nu)/d(h\nu)$ versus $(h\nu)$, there will be a peak at $E_g \approx h\nu$, where most of the transitions would occur. Fig. 4.7 (a) shows the plot of $d\, ln(\alpha h\nu)/d(h\nu)$ versus $(h\nu)$ for SB0, SB5, and SBN1 nanophosphors. The peak at a particular energy value on abscissa provides the approximate value of E_g. Consequently, by utilizing this approximate value of E_g, a graph of $\ln(\alpha h\nu)$ versus $ln(h\nu - E_g)$ is plotted to determine the value of n, as shown in Fig.4.8

(b). The slope of the linear part gives the value of n. The approximate band gap, estimated n values, and direct optical band gap of the doped and co-doped phosphors are tabulated in Table 4.4. The value of n was found to be about (1/2) for all the samples, evidencing that the absorption transition in the pure, doped, and co-doped Bi_2O_3 phosphors is the direct allowed transition[52,53,128].

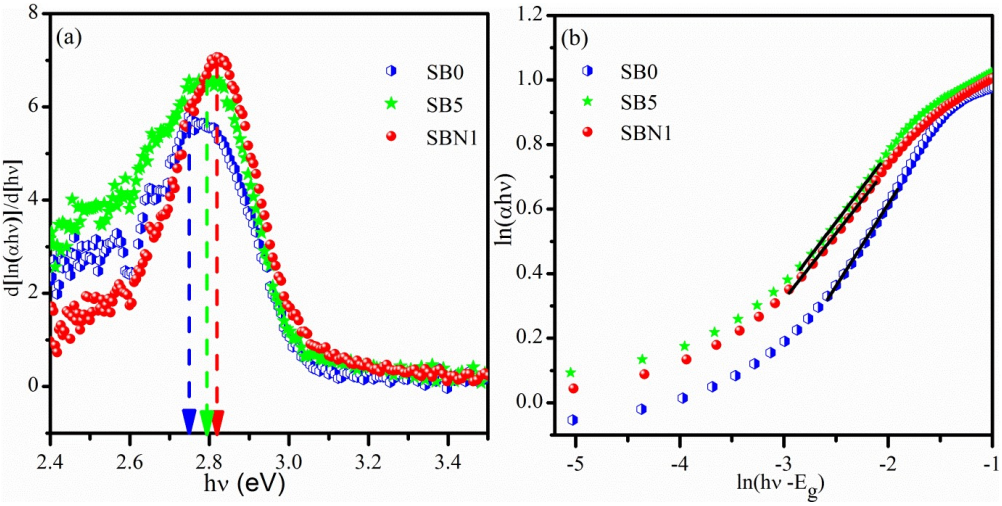

Fig. 4.7 (a) $d[ln(\alpha h\nu)]/d[h\nu]$ versus $h\nu$ and **(b)** $ln(\alpha h\nu)$ versus $\ln(h\nu - E_g)$ plots for SB0, SB5, and SBN1 nanophosphors.

Table 4.4 Approximate bandgap, n value, and direct optical band gap of SB0, SB5, and SBN1 nanophosphors.

Sample	Approximate band gap (eV)	n value	Direct band gap (eV)
SB0	2.749	0.53	2.725
SB5	2.799	0.43	2.784
SBN1	2.818	0.42	2.801

The estimated values (Table 4.5) suggest that the band gap of the phosphors initially increases (from 2.725 to 2.794 eV) with the doping of Sm^{3+} ions and further decreases (from 2.794 to 2.782 eV) with an increase in the Sm^{3+} doping concentration (from 1 to 7 mol%). The reduction in bandgap energy may arise due to the formation of intermediate

trap levels of Sm^{3+} within the bandgap region [129]. It is also seen that the co-doping of Na^+ leads to an augmentation in the bandgap from 2.784 to 2.807 eV. The band gap widening in the Sm^{3+} doped and Na^+ co-doped phosphors may arise due to the creation of ample carrier concentrations, which results in the Burstein-Moss shift [130,131]. Similar observations have been reported in our previous report also. However, the bandgap decreases (from 2.807 to 2.758 eV) with increasing Na^+ concentration in co-doped samples, and an apparent redshift is observed. This redshift in the bandgap may be due to the increase in oxygen vacancies originating from the substitution of Na^+ ions in the lattice [103,132,133]. The existence of oxygen vacancies in the Na^+ co-doped samples has been also confirmed by the XPS analysis. Thus, we can corroborate that the co-doping of Na^+ not only creates oxygen vacancies but also improves the crystallinity of the phosphors. To validate the formation of trap states, the Urbach energies are estimated using the relation [103],

$$\alpha = \alpha_o \, exp\left(\frac{h\nu}{E_U}\right) \tag{4.6}$$

The Urbach energies, summarized in Table 4.5, are obtained by linearly fitting the $ln\alpha$ v/s $h\nu$ plot and then taking the inverse of their slope. The Urbach energy plot for SBN1 phosphor is depicted in the inset of Fig. 4.8 (c). The estimated Urbach energy values and the existence of oxygen vacancies (depicted in XPS spectra) manifest the formation of localized trap states within the bandgap region in doped and co-doped samples and substantiate the obtained band gap results [69].

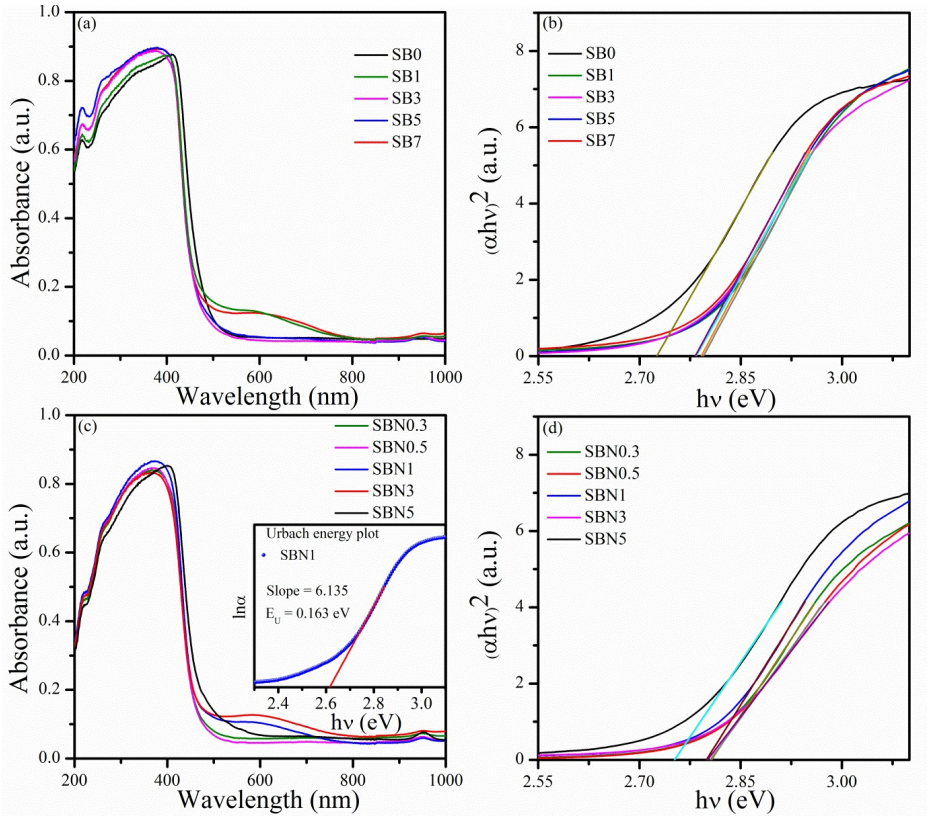

Fig. 4.8 (a, c) UV-Vis-NIR absorption spectra and **(b, d)** Tauc plots for prepared nanophosphors. The inset in **Fig. 7 (c)** depicts the Urbach energy plot for the SBN1 sample.

Table 4.5 Band gap (E_g) and Urbach energies (E_U) for all the samples.

Sample	E_g (eV)	E_U (eV)
SB0	2.725	0.193
SB1	2.794	0.170
SB3	2.792	0.172
SB5	2.784	0.175
SB7	2.782	0.176
SBN0.3	2.807	0.159
SBN0.5	2.805	0.160
SBN1	2.801	0.163
SBN3	2.800	0.178
SBN5	2.758	0.197

4.4.6 FTIR analysis

FTIR is a widely acceptable spectroscopic technique employed to investigate the chemical bonding and the functional groups in the synthesized nanostructures. Fig. 4.9 depicts the FTIR spectra of SB0, SB5, and SBN1, taken over the range of 400-4000 cm^{-1}. The peaks around 440, 570, 610, and 830 cm^{-1} are attributed to the characteristic stretching vibration of the Bi-O unit [128,134–136]. The existence of a small peak near 690 cm^{-1} in samarium containing phosphors is attributed to the Sm-O stretching [52]. However, the intensity of this peak reduced significantly in the Na^+ co-doped phosphors, which is favourable to enhance the PL emission intensity. The peaks located around 1370 cm^{-1} are accredited to the stretching vibration of nitrate ions which may arise due to the existence of nitrate group in the precursor and dopants, respectively [137,138]. The existence of peaks near 1650 and 1700 cm^{-1} corresponds to the stretching modes of hydrated O-H and C=O groups, respectively [52,139]. Moreover, the spectral band centered at 2350 cm^{-1} is assigned to the presence of adsorbed CO_2 molecules from the atmosphere, and the peak at around 2970 cm^{-1} is caused by the asymmetric stretching of C-H bonds [140–142].

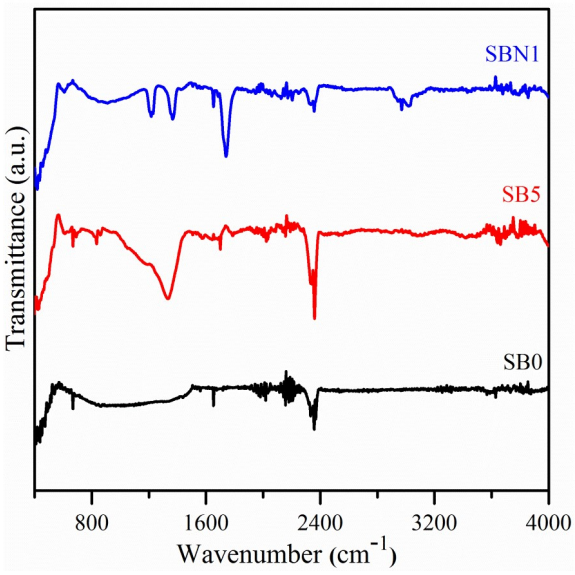

Fig. 4.9 FTIR spectra of SB0, SB5, and SBN1 nanophosphors.

4.4.7 PL studies

Photoluminescence spectroscopy is a prominent characterization technique, exploited to investigate the optical behaviour of the samples under different excitation and emission wavelengths. Fig. 4.10 (a, b) depicts the room temperature photoluminescence excitation (PLE) spectra of Bi_2O_3: Sm^{3+} and Bi_2O_3 :(Sm^{3+}, Na^+) nanophosphors, examined over the range of 360-500 nm, respectively. The sharp bands appearing at 365 nm ($6_{H_{5/2}} \rightarrow 4_{D_{\frac{3}{2},\frac{5}{2}}}$), 406 nm ($6_{H_{5/2}} \rightarrow 4_{F_{7/2}}$), 450 nm ($6_{H_{5/2}} \rightarrow 4_{G_{9/2}}$), 467 nm ($6_{H_{5/2}} \rightarrow 4_{I_{13/2}}$), 474 nm ($6_{H_{5/2}} \rightarrow 4_{I_{11/2}}$), and 481 nm ($6_{H_{5/2}} \rightarrow 4_{I_{9/2}}$) are assigned to the characteristic f-f transition of samarium ion and are found consistent with our previously reported results [88,103,129]. The prominent peak in the excitation spectra (at 481 nm) was used to explicate the emission behaviour of the synthesized nanophosphors.

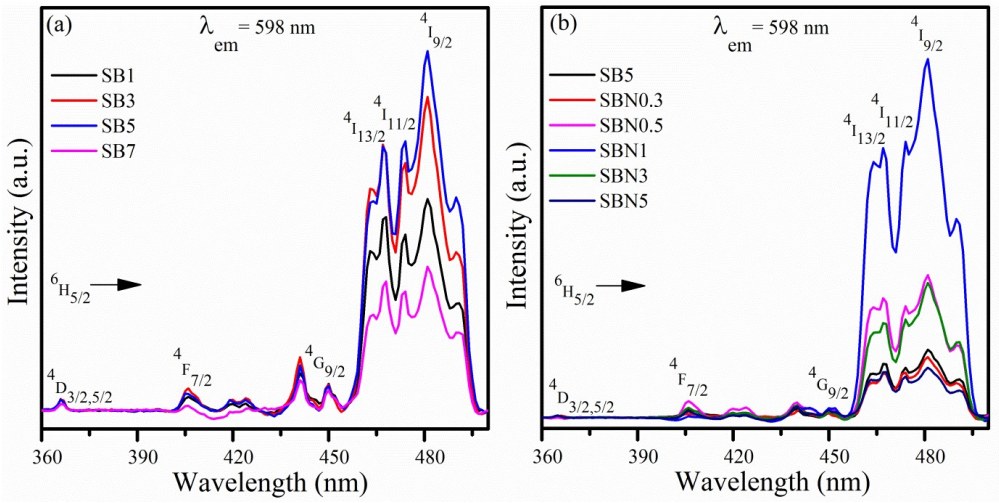

Fig. 4.10 PL excitation (PLE) spectra of **(a)** Sm^{3+} doped Bi_2O_3 and **(b)** Na^+ co-doped Bi_2O_3:(5%)Sm^{3+} nanophosphors at 598 nm emission wavelength.

The room temperature photoluminescence emission (PL) spectra (Fig. 4.11 (a, b)) of the samples were monitored at 481 nm excitation wavelength over the range of 540-740 nm. The spectra signify emission bands located at 564 nm (yellow), 598 nm (orange),

and 645 nm (red) involving multiple excited levels corresponding to $4_{G_{5/2}} \rightarrow 6_{H_{J/2}}$ ($J = 5, 7,$ and 9) transitions of Sm^{3+} activator ion.

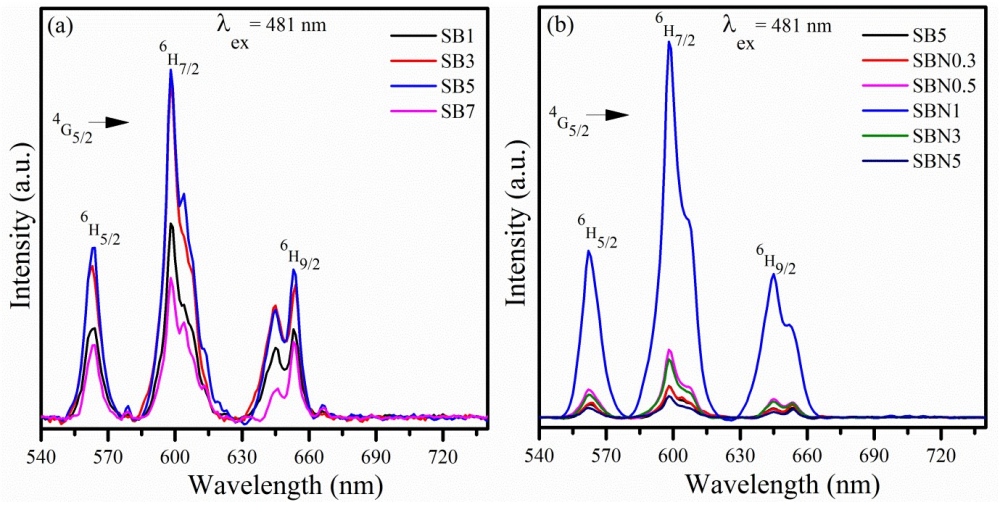

Fig. 4.11 PL emission spectra of **(a)** Sm^{3+} doped Bi_2O_3 and **(b)** Na^+ co-doped Bi_2O_3:(5%)Sm^{3+} nanophosphors at 481 nm excitation wavelength.

The peak centered at 645 nm ($4_{G_{5/2}} \rightarrow 6_{H_{9/2}}$) is assigned to electric dipole (ED) transition (selection rule $\Delta J \geq \pm 2$), which is highly sensitive to the local crystal field ambience. The peak at 564 nm ($4_{G_{5/2}} \rightarrow 6_{H_{5/2}}$) is consistent with magnetic dipole (MD) transition ($\Delta J = 0, \pm 1$) and is less sensitive to the crystal field environment around the activator ions. The integrated intensity ratio of ED transition to the MD transition is defined as the asymmetry ratio ($R_{asy} = I_{ED}/I_{MD}$) and measures the extent of deviation from the symmetry of inversion around the activator ions in the host matrix [143]. The estimated values of R_{asy} for SB5 and SBN1 are 1.23 and 1.38, respectively. The increased asymmetry ratio suggests that the symmetry around the Sm^{3+} ions decreases with Na^+ co-doping and Sm^{3+} ions are sitting at the lower symmetry sites and eventually the PL red emission intensity is enhanced [144,145]. Moreover, the enhancement in emission intensities in co-doped nanophosphors can be attributed to the improvement in the crystalline nature. The co-doping of Na^+ leads to an enhancement in the crystallite size,

which results in a decrease in surface to volume ratio of the nanophosphors. Thus, the available luminescence quenching centers on the surface of nanophosphors are reduced, and hence, the non-radiative relaxation probabilities are reduced [146,147].

From Fig. 4.11 (a), it is evident that the emission intensity increases upon increasing the concentration of Sm^{3+} ions. The emission intensity reaches a maximum for SB5 sample and thereafter decreases on further increasing the Sm^{3+} concentration owing to concentration quenching. Thus, SB5 (5% Sm^{3+} doped Bi_2O_3) is the optimum concentration for Sm^{3+} doped samples and this concentration was further used for the co-doping of Na^+ ions. The concentration quenching phenomena at higher doping concentrations may take place as a consequence of the non-radiative energy transfer, arising either due to exchange interaction or multipolar interaction. The exchange interaction arises when the critical distance (R_c) between neighbouring dopant ions is lower than ~ 5Å.

The critical distance (R_c) between the activator ions is calculated using the Blasse relation [54,144] given by,

$$R_c = 1.24 \times \left(\frac{V}{x_c N}\right)^{\frac{1}{3}} \tag{4.7}$$

Where, V is the unit cell volume, x_c represents the critical dopant concentration and N denotes the number of cation sites available for the activators in the host lattice. In our case, x_c = 0.05 and N = 8. The estimated critical distance for SB5 nanophosphor was found to be 11.65 Å, which is larger than 5 Å. Thus, the possible resonance energy transfer in our samples is due to the multipolar interaction. The optimal Sm^{3+} concentration was further used for the co-doping of Na^+ ions and we observed a nearly ten-fold enhancement in the fluorescence intensities for SBN1 nanophosphor, as

compared to the SB5 nanophosphor. However, at higher co-doping concentrations, the co-activator ions may tend to create an excess amount of adsorbed oxygen vacancies on the surface of the phosphors, which may act as luminescence quenching centers. As a result, the probability of non-radiative transitions is increased and the emission intensity is decreased [143].

In our previous work, we have reported a two-fold augmentation in the fluorescence intensity of Sm^{3+} ion in Bi_2O_3 after Li^+ co-doping [103]. However, in the present work, we have achieved a ten-fold enhancement in the emission intensity after Na^+ co-doping. The additional increase in fluorescence intensity in Na^+ co-doped phosphor can be ascribed to the fact that the ionic radius of Na^+ ion (1.02 Å) is comparable to the Bi^{3+} ion (1.03 Å), therefore they can easily accommodate the substitutional sites and create minimal lattice distortion. Whereas, the ionic radius of Li^+ ion (0.76 Å) is comparably smaller than the Bi^{3+} ions, therefore they occupy substitutional as well as interstitial positions and create larger lattice distortions. Moreover, an increased crystal field asymmetry in the Na^+ co-doped phosphors as compared to our previous work on Li^+ co-doped phosphors also helps in improving the emission intensity. Similar trends for improved emission intensity in Na^+ co-doped phosphors as compared to other alkali metal ions have been also reported by J Wu *et al.* and T. Deng *et al.* [148,149].

The schematic energy level diagram, involving possible multiple transitions in the Sm^{3+} ion for the prepared nanophosphors is illustrated in Fig. 4.12.

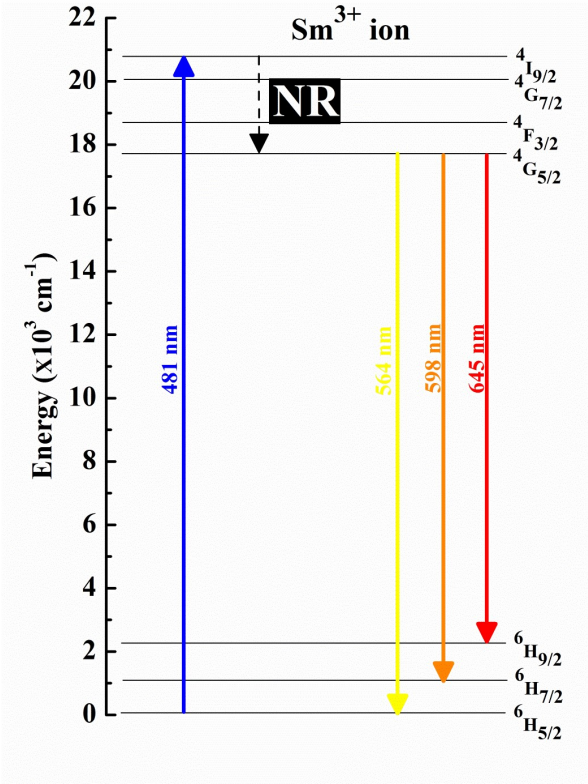

Fig. 4.12 Schematic energy level diagram of activator Sm^{3+} ion.

4.4.8 Decay curve analysis

Figs. 4.13 (a, b) depict the normalized PL decay curves of $4_{G_{5/2}} \rightarrow 6_{H_{7/2}}$ transition (598 nm), excited at 481 nm for SB5 and SBN1 nanophosphors, respectively. The decay curves fit well with the biexponential function given by the equation [150],

$$I(t) = I_o + A_1 exp\left(-\frac{t}{\tau_1}\right) + A_2 exp\left(-\frac{t}{\tau_2}\right) \quad (4.8)$$

Where I_o and I are the intensities at time 0 and after t seconds. A_1 and A_2 are the fitting parameters. τ_1 and τ_2 represent the rapid and slow decay time components, respectively. The average lifetime of the phosphors can be evaluated by the relation [150],

$$\tau_{avg} = \left(\frac{A_1\tau_1^2 + A_2\tau_2^2}{A_1\tau_1 + A_2\tau_2}\right) \quad (4.9)$$

Using the above equations, the average lifetime of $4_{G_{5/2}}$ level of the Sm^{3+} ion for SB5 and SBN1 phosphors is found to be 461 and 493 μs, respectively. This shows an augmentation in the lifetime of $4_{G_{5/2}}$ level, which may arise due to the improvement in crystallinity and decrease in luminescence quenching centers upon Na^+ co-doping [7].

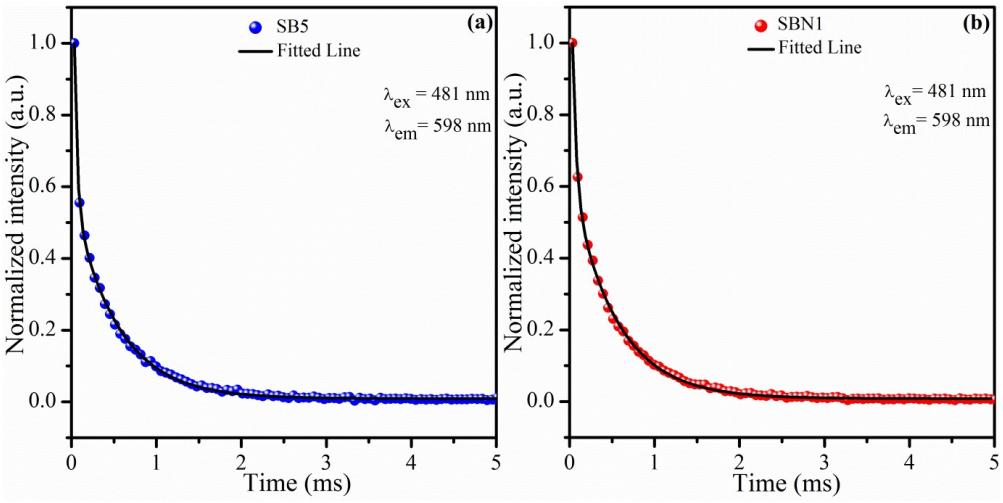

Fig. 4.13 Normalized PL decay curves of (a) SB5 and (b) SBN1 nanophsophors.

4.4.9 Temperature-dependent PL study

The study of thermal stability of the phosphors is essential in order to investigate its luminescence properties and suitability for various technological applications in high-temperature environments. Fig.4.14 (a) demonstrates the temperature-dependent PL emission spectra of SBN1 phosphor in the temperature range 303–453 K under 481 nm excitation. The integrated emission intensity decreases as the operating temperature increases from 303 K to 453 K due to the thermal quenching effect. At 423 K, the emission intensity is 55.29% of the intensity at 303 K, suggesting that the prepared Na^+ co-doped nanophosphors have good thermal stability at high temperatures (Fig. 4.14 (b). The configurational coordinate diagram provides a better understanding of the thermal quenching process and is displayed in Fig. 4.14 (c). At normal temperatures, electrons of the Sm^{3+} ion in the ground state (^6H) absorb the incident photon energy and jump to the

excited state (^4G) from point A to B via path (1). Thereafter, they come to the equilibrium position (point C) via non-radiative relaxations and ultimately revert to the ground state by emitting radiative photons following path (2). As the temperature is elevated, some of the excited electrons couple with the thermally active phonons and attain sufficient energy to overcome the activation energy barrier E_a and reach point D (intersection point of ground and excited states), thereby relaxing non-radiatively to reach the ground state (path (3)). This phenomenon leads to a reduction in the emission intensity of the phosphors at elevated temperatures [151]. Moreover, the activation energy E_a was evaluated by employing the Arrhenius equation [152],

$$I_T = \frac{I_0}{1 + Ce^{(-E_a/KT)}} \tag{4.10}$$

Where I_T and I_0 represent the PL intensities at temperature T and 303 K, respectively; K (8.629 x 10^{-5} eV/K) is the Boltzmann constant, and C is a constant. The $ln\left(\frac{I_0}{I_T} - 1\right)$ vs. $1/KT$ plot, depicted in Fig. 4.14 (d), is fitted linearly and its slope gives the value of E_a. The obtained value of E_a is 0.23 eV. In addition, the effect of increasing temperature on emission color was investigated by evaluating the CIE chromaticity coordinates of the SBN1 phosphor at different temperatures. From Fig. 4.15 (a), it is evident that the color coordinates do not change significantly at high temperatures, which suggests that the prepared phosphor has a stable emission colour at different working temperatures and therefore it is a suitable choice for various lighting and display device applications.

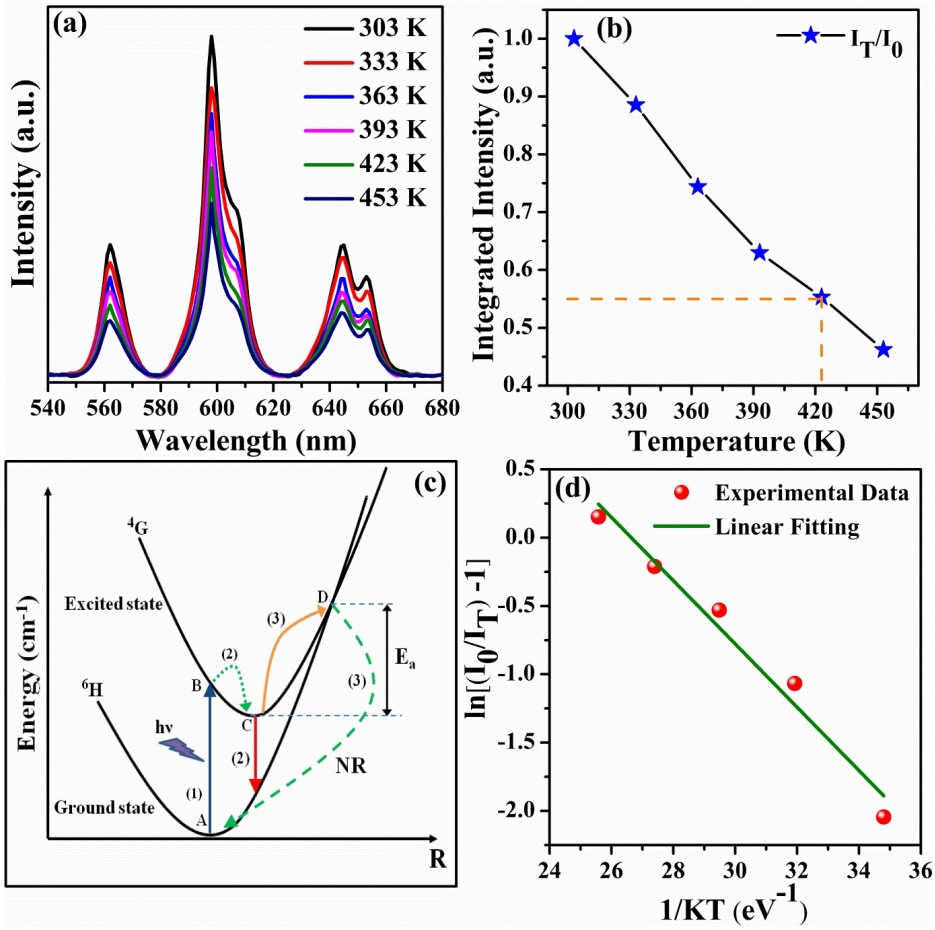

Fig. 4.14 (a) Temperature-dependent PL spectra, **(b)** Normalized integrated intensity plot as a function of temperature, **(c)** Configurational coordinate diagram for understanding thermal quenching phenomenon, and **(d)** $\boldsymbol{ln\left(\frac{I_0}{I_T}-1\right)}$ vs. $\boldsymbol{1/kT}$ plot for the determination of activation energy for SBN1 nanophosphor.

4.4.10 CIE and CCT analysis

Fig. 4.15 (b) displays the Commission International de L'Eclairage (CIE) chromaticity diagram and the corresponding CIE coordinates of SB5 and SBN1 nanophosphors. The estimated CIE co-ordinates for SB5 and SBN1 are (0.499, 0.498), (0.558, 0.441), respectively. The corresponding correlated colour temperature (CCT) of the samples was calculated using the empirical McCamy relation [153],

$$CCT = -449n^3 + 3525n^2 - 6823n + 5520.33 \qquad (4.11)$$

Where (x, y) is the CIE coordinate, (x_e, y_e) is the chromaticity epicenter having coordinates (0.338, 0.186), and $n = \left(\frac{x-x_e}{y-y_e}\right)$ is the inverse slope line,. The obtained CCT values for SB5 and SBN1 were found to be 2808 K and 1969 K, respectively. The lower CCT ascertains that the Na^+ co-doped phosphors are potential candidates to procure energy-efficient warm wLEDs and display devices.

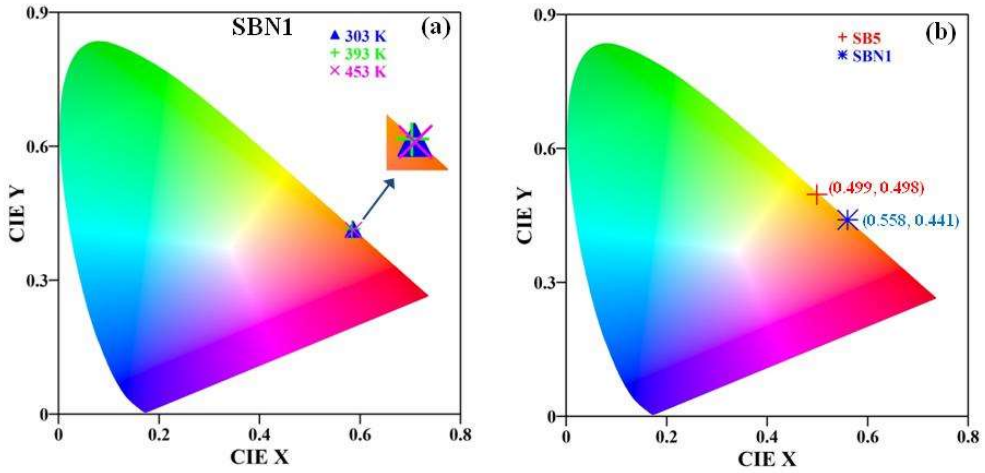

Fig. 4.15 CIE chromaticity diagrams depicting (a) variation in CIE coordinates with temperature for SBN1 nanophosphor, and (b) variation in CIE coordinates at room temperature for SB5 and SBN1 nanophosphors.

4.5 Conclusions

This chapter focuses on the facile and room temperature synthesis of Sm^{3+} doped and alkali metal (Na^+) co-doped Bi_2O_3 nanophosphors using co-precipitation method, including the study of their structural and optical properties. The XRD results reveal the monoclinic crystal structure of the prepared nanophosphors. An improved crystallinity is observed in co-doped samples, which also helps in improving the PL emission intensity. The HR-SEM analysis suggests that the prepared nanophosphors have nano-sheet-like morphology. The corresponding EDX spectra confirm the presence of all elements in the phosphors. The TEM images substantiate the nano-sheet-like morphology, obtained from the HR-SEM micrographs and confirm the polycrystalline nature of the phosphors. The

XPS analysis confirms the presence of all the elements, validates their oxidation states, and verifies the EDX data. The UV-Vis absorption spectroscopy reveals the decrease in the bandgap of the phosphors with the increase in doping and co-doping concentrations, which may arise due to the formation of intermediate trap levels within the bandgap region and increased oxygen vacancies. These results were further validated by the corresponding Urbach energy values. The FTIR spectra give information about the bonding states of the chemical species and the functional groups present in the synthesized nanophosphors. The PL emission studies were carried out at 481 nm excitation and the maximum emission corresponding to $4_{G_{5/2}} \rightarrow 6_{H_{7/2}}$ transition was observed at 598 nm. The fluorescence intensities were found to increase nearly ten-fold in SBN1 nanophosphor, as compared to the SB5 nanophosphor. The obtained CCT values for SB5 and SBN1 were found to be 2808 K and 1969 K, respectively. This implies that co-doping leads to a significant decrease in the CCT. Thus, we can corroborate that the co-doping of Na^+ ion leads to a substantial enhancement in the luminescence intensity of the rare-earth-doped nanophosphors, and therefore, they can have potential applications in solid-state lighting and display devices. The decay curves analysis further supports the enhancement in emission intensity for 1% Na^+ co-doped phosphor. The temperature-dependent PL analysis reveals that PL emission decays by ~ 44.7% at 423 K (150℃) and the thermal activation energy was calculated to be 0.23 eV